

Spidroin-Inspired Hierarchical Structure Binder Achieves Highly Integrated Silicon-Based Electrodes

Pengzhou Mu

Qingdao Institute of Bioenergy and Bioprocess Technology, College of Materials Science and Opto-Electronic Technology, University of Chinese Academy of Sciences, Shandong Energy Institute

Shu Zhang

Qingdao Institute of Bioenergy and Bioprocess Technology, College of Materials Science and Opto-Electronic Technology, University of Chinese Academy of Sciences

Huanrui Zhang

Qingdao Institute of Bioenergy and Bioprocess Technology, College of Materials Science and Opto-Electronic Technology, University of Chinese Academy of Sciences, Shandong Energy Institute

Jiedong Li

Qingdao Institute of Bioenergy and Bioprocess Technology, Chinese Academy of Sciences

Zhi Liu

Qingdao Institute of Bioenergy and Bioprocess Technology, College of Materials Science and Opto-Electronic Technology, University of Chinese Academy of Sciences, Shandong Energy Institute

Shanmu Dong

Qingdao Institute of Bioenergy and Bioprocess Technology

Guanglei Cui

cui-gl@qibebt.ac.cn

Qingdao Institute of Bioenergy and Bioprocess Technology, College of Materials Science and Opto-Electronic Technology, University of Chinese Academy of Sciences, Shandong Energy Institute

<https://orcid.org/0000-0001-5987-7569>

Article

Keywords:

Posted Date: March 8th, 2023

DOI: <https://doi.org/10.21203/rs.3.rs-2634709/v1>

License:  This work is licensed under a Creative Commons Attribution 4.0 International License.

[Read Full License](#)

Additional Declarations: There is **NO** Competing Interest.

Version of Record: A version of this preprint was published at Advanced Materials on October 10th, 2023. See the published version at <https://doi.org/10.1002/adma.202303312>.

Abstract

As a promising component for next-generation high energy lithium-ion batteries, silicon based electrode has attracted increasing attention by virtue of ultrahigh theoretical specific capacities. Nevertheless, fast capacity fade posed by tremendous volume changes during the lithiation and delithiation process remains a huge challenge before large-scale applications. Inspired by spidroin, we herein develop a tenacious hierarchical structure binder for tolerating huge volume change of silicon-based anode, which is prepared through simply mixing aqueous poly(acrylic acid) solution, and oily *N*-methyl pyrrolidone solution containing a tetrazole groups based copolymer (PPB) of polyacrylonitrile and poly(ethylene glycol) bisazide. Such an aqueous-oil binary solution based blend (AOB) binder exhibits a spidroin-like hierarchical structure. In the AOB binder, hydrophobic PPB polymer condensates in the mixture solution to form crystalline region within submicron-sized irregular spherical domains as the rigid node of the molecular chain segment similar to β -sheet of spidroin; while water-soluble, amorphous poly(acrylic acid) mimicks the α -helix structure of spidroin, and builds up a network structure by linking with PPB via ionic bonding similar to the interactions between repetitive amino acid sequence segment in the primary structure of spidroin. Benefited by these, AOB binder enables both high tensile strength and elasticity, and superior adhesion of electrodes, therefore apparently stabilizing silicon-based anode structure and rendering prolonged electrode cycle life. This work marks a milestone in developing state-of-the-art silicon-based electrodes towards high energy density lithium battery applications.

Introduction

Developing novel electrode materials is vital for meeting the ever-growing energy density demand of lithium batteries in electric vehicles and portable electronic devices applications.¹⁻³ Thus far, silicon (Si) has been well recognized as the promising active material owing to its high theoretical specific capacity (~ 4200 mAh/g) and natural abundance.^{4,5} Despite these good strengths, the commercialization of these active materials based electrodes is still significantly restricted mainly due to a series of challenging problems below. Firstly, the huge volume expansion ($\sim 300\%$) and shrinkage during cycling results in the active particle pulverization, exfoliation of electrode films, and uncontrollable growth of electrode/electrolyte interphase; these negative factors render fast decline of battery capacity along with low Coulombic efficiency. Secondly, poor ionic and electronic conductivity of active materials increases the irreversible degree of lithiation and delithiation, which renders low initial Coulombic efficiency and inferior rate capabilities.⁶ All these challenges bring about poor cycling performance and hinder the commercial implementation of high-capacity Si-based anode in rechargeable lithium ion batteries (LIBs).

Over the years, several pathways including material structure optimization, electrolyte engineering and polymeric binder exploitation have been proposed to alleviate the aforementioned cycling stability issues of Si-based anodes.⁷⁻¹⁰ Among them, the development of advanced binder is deemed as a simple yet powerful way since it bonds active material and conductive additive onto current collector and plays a pivotal role in maintaining structural integrity of electrodes during charge/discharge processes. There is a

growing consensus that the development of binders with both high elastic modulus and stretchability helps mechanically match with volume change of Si electrodes and thus achieve their extended cycling life.^{11–13} Toward this end, rational structure design of polymer binder is of great significance. As yet, numerous polymer binders featuring various polar groups (e.g. –COOH, –OH and –CONH₂) and linear, comb shaped or crosslinked network polymer backbones have been developed to ameliorate Si-based electrode cycling performance.^{14–17} For instance, linear poly(acrylic acid) (PAA), polyacrylamide (PAM), polyvinylidene fluoride (PVDF), polyurethane (PU) and polysaccharides [e.g. sodium carboxymethyl cellulose (CMC) and alginate] have shown relatively improved cycling life of Si-based electrodes.^{18,19} However, these polymer binders can hardly effectively address the aforementioned issues confronted by Si-based electrode, mainly owing to their large elongation at break accompanied by low elasticity modulus (e.g. PVDF, PU) or vice versa (e.g. PAA, CMC) when plasticized by liquid electrolyte within LIBs. Meanwhile, constructing chemically crosslinked network binders by introducing reactive linkers has been employed to regulate the mechanical tradeoff of linear binders.^{20–22} Nevertheless, the crosslinking reaction generally complicates electrode preparation process, and worse yet, crosslinked binders with excellent mechanical match capabilities remain scarce. Given the drawbacks of the topological structure design mentioned above, it is evident that arousing the hierarchical structure design of polymer materials is helpful to decouple the mechanical tradeoff; however, rare of previously reports have focused on this pivotal factor for Si-based anode binder to the best of our knowledge.

Spidroin is a natural high-molecular-weight protein (typically 250–400 kDa) secreted by dedicated glands of arthropods, which convert viscous proteinaceous aqueous solutions into such a light, solid biofibre. The most attractive point for spidroin is that it can achieve perfect mechanical matching and wonderful shape recovery, which can withstand the impact of prey and entangle flying insects and maintain the structural integrity of the web. These benefits are highly correlated to the unique hierarchical structure of spidroin: (1) In the primary structure, spidroin generally consists of a highly repetitive amino acid sequence segment flanked by amino- and carboxyl-terminal domains (NTD and CTD, respectively), which can form ionic bonding themselves to improve mechanical toughness. (2) Its higher order structure is composed of crystalline β -sheet and amorphous α -helix; polyalanine folds to form β -nanocrystals during spider drawing process attributable to its hydrophobicity, contributing to the high strength of spidroin, while another water-soluble polyamino acid (e.g., polyglycine) chain forms a loose α -helix structure to connect the β -nanocrystals (Fig. 1a). Learning from the hierarchical structure of spidroin, we propose a novel aqueous-oil binary solution based blend (AOB) binder for Si electrodes. The as-developed binder is prepared by simply mixing aqueous poly(acrylic acid) (PAA) solution, and oily *N*-methyl pyrrolidone (NMP) solution containing a copolymer (PPB) of polyacrylonitrile (PAN) and poly(ethylene glycol) bisazide (N₃ – PEO – N₃). Hydrophobic PPB condensates in the mixture solution to form crystalline regions within submicron-sized irregular spherical domains as the rigid node of the molecular chain segment similar to β -sheet of spidroin; while water-soluble, amorphous PAA mimicks the α -helix structure of spidroin, and builds up a network structure by linking with PPB via ionic bonding similar to the interactions between NTD and CTD in the primary structure of spidroin (Fig. 1b). The hierarchical structure design endows the as-developed binder with high tensile strength and elasticity, as well as

excellent self-healing abilities. Therefore, compared with traditional binders (e.g. PAA), AOB binder can better accommodate enormous electrode volume deformation and more effectively stabilize the electrode/electrolyte interface upon lithiation/delithiation (Fig. 1c-d). As a result, nano-Si electrode and Si/C composite electrode S600 [contains SiO_x ($0 < x < 1$)], a specific capacity of 600–650 mAh/g at 0.1 C] with the AOB binder exhibit superior long cycle stability and rate performance to traditional PAA binder. Impressively, in 3.3 Ah soft package cells assembled with commercially available S600 anode and NCM811 cathode, a discharge specific capacity of 2.92 Ah after 700 cycles with a capacity loss of 0.013%/cycle can be maintained, undoubtedly confirming the utility of AOB binder. The polymer binder hierarchical structure design philosophy provides an important route to advance practical implementation of high specific capacity Si-based electrodes.

Experimental Section

Materials

Azide-polyethylene glycol–azide ($M_n = 2000$ Da) was obtained from Xi'an Ruixi Biological Technology Co., Ltd. Si nanoparticles (~ 200 nm) were purchased from Guangtong Quzhou New Material Technology Co., Ltd. PAN ($M_n = 150$ KDa), acetone, polyacrylic acid (PAA, $M_n = 450$ KDa), NMP, *N,N*-dimethylformamide (DMF, 99.9%), dimethylsulfoxide- d_6 (DMSO- d_6) were purchased from Sigma-Aldrich Inc. 1 M LiPF_6 in ethylene carbonate (EC)/dimethyl carbonate (DMC) (1:1, v/v) was purchased from Duoduo Reagent Co., Ltd. Fluoroethylene carbonate (FEC) was purchased from Aladdin Inc.

Preparation of PPB

Typically, the tetrazole-based polymer PPB was obtained by dissolving 2.0 g PAN powder and 0.08 g poly(ethylene glycol) bisazide in a solution comprised of 9.4 g DMF and 1.9 g acetone in an oil bath under 140 °C overnight. By adding the mixture into ethanol solution dropwise, the precipitate was formed. The crude product was collected through centrifugation for 20 min at a speed of 4000 r/min. Then by dissolving the crude product in DMF again and repeating this dissolution/precipitation process three times, the final precipitate was dried in an oven at 60 °C for 24 h to give the pure polymer PPB.

Preparation of AOB, PAB-N, and PAB-W binders

AOB binder was prepared by aqueous-oil binary mixing process. Specifically, AOB binder solution (5 wt%) was obtained by mixing pre-prepared aqueous PAA solution and oily NMP solution containing PPB in a given ratio. While PPB and PAA were mixed in sole water and sole NMP to form 5 wt% PAB-W binder and PAB-N binder solutions, respectively.

Preparation of electrodes: The Si based-anode slurry contains active material (200 nm Si or S600), Super P and binder (PAA, AOB binder) with a mass ratio of 8:1:1, which was blade-coated on a Cu current collector. After drying at 60°C for 2 hours and 120°C for 12 hours under vacuum, the anodes were cut into wafers with a 14 mm diameter. $\text{LiNi}_{0.8}\text{Co}_{0.1}\text{Mn}_{0.1}\text{O}_2$ (NCM811) electrode consisting of active material,

super P, and PVDF in a weight ratio of 8:1:1 was used as the full coin cell cathode and its diameter is 12 mm. To assemble soft package full cells, NCM811 cathode was fabricated by preparing a slurry consisting of NCM811, super P, and PVDF in a weight ratio of 94:3:3 in NMP. The slurry was cast onto aluminum foil and dried under vacuum. The S600 anode slurry contains active material, Super P and AOB binder with a mass ratio of 90:3:7, which was blade-coated on a Cu current collector and dried under vacuum.

Sample characterization

$^1\text{H-NMR}$ and $^{13}\text{C-NMR}$ spectroscopies were performed to analyze the polymer structure on a Varian 600 MHz Gemini, and the DMSO- d_6 was used as the solvent. In addition, the Fourier transform infrared (FT-IR, Bruker VERTEX 70) spectrum was also used to characterize the structure of different polymers. Temperature-dependent IR spectroscopy was measured on Thermo iS10 and the sample was prepared by spin-coating the AOB binder solution on KBr, while the corresponding data was collected upon heating with the temperature ranging from 30 to 100°C. Nano-indentation test was carried out using Bruker Hysitron TI980 nanoindentation system with normal Berkovich indenter. The tensile and peeling tests of AOB binder films were analyzed by using a universal testing machine (MTS, E43). For tensile testing analysis, the polymer films were prepared by drying the polymer solutions at 120°C overnight and then cut into 1 cm \times 5 cm. Using the same MTS, 180° peeling test was conducted to evaluate the peel strength of each electrode. The electrode was cut into a rectangular shape with 2 cm \times 7 cm. The active material side was adhered to a wood bar by using 3M double sided adhesive tapes, and meanwhile the collector side was adhered by using traditional 3M tapes. The peel strength value would be output directly to a computer. The swelling of the binder film in liquid electrolyte was examined gravimetrically by soaking the binder film into the liquid electrolyte before and after 24 hours. Contact angles of different binder solutions on monocrystalline Si were measured by using DSA100. The in-situ optical microscope (Cossim CMY-400Z optical microscope) was used to observe the cross-section of Si electrode with different binders in real time in order to study the electrode deformation process during battery cycling. Top-viewed and cross-sectional images of the electrodes were obtained by using scanning electron microscopy (SEM, Hitachi S-4800) and cross-sectional ion milling scanning electron microscopy (IM-SEM, Hitachi IM4000PLUS), respectively. X-ray photoelectron spectroscopy (XPS) analysis was carried out using Thermo Fisher ESCALAB XI + spectrometer equipped with an Al K α source.

Cell assembly and electrochemical measurements

Coin-cells (S600/Li, Si/Li, NCM811/nano-Si and NCM811/S600) were assembled in a 2032-coin cell device within a glove box containing less than 0.01 ppm water and O $_2$, and measured on Land battery test system (Land CT2001A, Wuhan Land Electronic Co. Ltd., China). The microporous polypropylene film (Celgard 2500) was performed as the separator. Commercially available 1.0 M LiPF $_6$ in EC/DMC/FEC (4.5/4.5/1, v/v/v) was used as the electrolyte. To assemble NCM811/S600 and NCM811/nano-Si full-cells, the n/p ratio was 1.2. The Si based anodes were pre-charged and pre-discharged for three cycles at a current density of 0.1 C. Soft package cells' fabrication was conducted in a dry room with a dew point

of $-40\text{ }^{\circ}\text{C}$. The details of the soft package cell were shown in Table S3. Soft package cells used commercial NCM811 cathode (a mass loading of 16 mg/cm^2 on each side) and S600 anode (a mass loading of 5.5 mg/cm^2 on each side), the n/p ratio was 1.15 and the electrolyte employed commercially available 1 M LiPF_6 in EC/DMC/FEC (4.5/4.5/1, v/v/v) with a dosage of 2.7 g/Ah . Cyclic voltammetry (CV) measurements for Si anode were conducted on cells using BioLogic VSP-300 conducted at a scan rate of 0.5 mV/s at room temperature. Electrochemical impedance spectroscopy (EIS) measurements in the frequency range from 100 mHz to 7 MHz were carried out on BioLogic VSP-300 to compare the impedance.

Calculations

DFT calculations were conducted using the Gaussian09 software. All the molecules were pre-optimized at the B3LYP levels of theory with the 6-311 + G(d, p) basis set. The single point energy was calculated based on the same function with 6-311 + G(d, p).

The bonding energies (ΔE) were calculated using the following formula:

$$\Delta E = E_{A+B} - E_A - E_B$$

where E_{A+B} is the total energy of the system, E_A and E_B are the energy of the isolated molecules.

In addition, the finite element analysis (FEA) simulation was conducted by COMSOL Multiphysics 5.6. The Si anode was simplified as a typical two-phase composite material with Si particles embedding in the binder. The stress distribution induced by Li insertion process follows $\rho \frac{\partial^2 L}{\partial t^2} = \nabla \cdot (C : \varepsilon_{el})$, where $C = C(E, \nu)$ is the fourth-order elastic tensor, E is the Young's modulus, and ν is the Poisson's ratio; ε_{el} is the elastic strain which can be described by the following equation

$$\varepsilon_{el} = \frac{1}{2} \left[(\Delta L)^T + \nabla L \right] - \beta_h M (c - c_{ef})$$

where L is the displacement, β_h is the expansion coefficients, M is the molar mass, c_{ef} is the reference concentration, ∇ is the divergence, and Δ is the Laplace operator. In the static stress analysis, the mechanical properties of different binders were obtained from experimental results. The corresponding parameters were shown in Table 1.

Table 1
Parameters of different binders for FEA simulation.

Parameter	Dimension	Value	Description
E_Si	GPa	152.2	Young's modulus of Si
v_Si	1	0.21	Poisson's ratio of Si
ρ_{Si}	g/cm ³	2.236	Density of Si
E_PAA binder	MPa	144	Young's modulus of PAA
v_PAA binder	1	0.44	Poisson's ratio of PAA
$\rho_{\text{PAA binder}}$	g/cm ³	1.09	Density of PAA
E_AOB binder	MPa	310	Young's modulus of AOB binder
v_AOB binder	1	0.4	Poisson's ratio of AOB binder
$\rho_{\text{AOB binder}}$	g/cm ³	1.2	Density of AOB binder

Results and discussion

Hierarchical structure design of AOB binder

To mimic the hierarchical structure of spidroin, it starts with designing the binder topological structure with dynamic ionic bonding. To accomplish this, polymer design based on acid-base interaction is a viable route. As mentioned above, traditional water-soluble binder PAA usually suffers from large elasticity modulus yet low elongation at break at ambient temperature, leading to irreversible electrode film fracture and thus fast degradation of cycling performance.^{23,24} To improve the elongation at break of PAA, it is hopeful to introduce other polymers that can construct dynamic ionic bonding with it.^{25,26} As a typical nitrogen-rich heterocyclic backbone, tetrazole group is an excellent proton acceptor with multiple coordination sites to form acid-base interactions.^{27,28} Another benefit is that the conjugated tetrazole structure can form reversible lithiation sites, beneficial to transport lithium ions and thus to improve rate performance of lithium batteries.^{29,30} As a consequence, a robust binder system with a strong dynamic ionic bonding network can be constructed by mixing PAA with a tetrazole groups-containing polymer.

Therefore, a hydrophobic, tetrazole groups-containing polymer PPB consisting of PAN and PEG segments was designed, both of which help improve elasticity and meanwhile conduct lithium ions. A synthesis schematic diagram of PPB is shown in Fig. 2a. Via a simple "click" reaction between $-\text{CN}$ and $-\text{N}_3$ groups, PPB was obtained via thermally induced cycloaddition of $\text{N}_3 - \text{PEO} - \text{N}_3$ and PAN under 140 °C.³¹ This reaction occurred smoothly, as evidenced by the peak change of $-\text{CN}$ and $-\text{N}_3$ groups in ¹H-NMR, ¹³C-NMR and FTIR spectra (Figure S1-3). Meanwhile, the N 1 s XPS spectrum further supports this result;

four peaks generate corresponding to N = C at 398.7 eV, N - C at 400.4 eV and ⁺HN - C bonding at 401.5 eV on tetrazole units (Figure S4).^{32,33}

In the AOB binder (Fig. 2a), the strong ionic bonds between tetrazole with carboxyl motifs was confirmed through FTIR spectra (Fig. 2b). For PAA, the stretching vibrational absorption peaks of -OH, C = O, C - O are located at 2500 ~ 3000 cm⁻¹, 1708 cm⁻¹ and 1242 cm⁻¹, respectively. Tetrazoles in PPB contain four nitrogen atoms as coordination sites, which can all act as carboxylic proton acceptors to form hydrogen bonding. After mixing with PPB, the weakened absorption peak of C = O in PAA accompanied by an obvious redshift (1708 → 1677 cm⁻¹) occurs, indicating that the carboxylic acid in PAA coordinates with nitrogen atoms of tetrazoles in PPB forming tight ionic bonding NH⁺•••⁻O - C = O. Meanwhile, the characteristic peak intensity of C - O in carboxylic acid of PAA and of C - N in tetrazoles of PPB enhances, accompanied by apparent blueshifts (1242 → 1265 cm⁻¹, 1163 → 1172 cm⁻¹, respectively). Furthermore, the peak intensity of -OH in PAA becomes weak and a new peak (2700 cm⁻¹) generates due to the generation of -NH⁺ on tetrazoles. Temperature-dependent real-time IR analysis was employed to further demonstrate the presence of such ionic bonding in AOB binder. As shown in Fig. 2c, with the increase of temperature, the peaks ascribed to C - N, C = O and C - O stretching vibration gradually shift from ~ 1172 to ~ 1164 cm⁻¹, from ~ 1670 to ~ 1700 cm⁻¹ and from ~ 1265 to ~ 1225 cm⁻¹, respectively (Fig. 2c), suggesting that the breakage of NH⁺•••⁻O - C = O and hydrogen bonding involving carboxyl, and the generation of a mass of free carboxylic and tetrazole groups. Evidently, the dynamically reversible ionic bond network within AOB binder helps dissipate stress and thus can accommodate enormous electrode volume deformation.³⁴

Further theoretical calculation shows that the ionic bond energy between every N of tetrazole with carboxyl group is similar (ranging from - 11 to - 14 kcal mol⁻¹), but much larger than the hydrogen bonding formed between carboxyl groups themselves (-4.7 kcal mol⁻¹) (Fig. 2d). It has been extensively established that such ionic bonding can reconstruct at shattered interfaces, restoring the mechanical strength and original shape of materials.³⁵ Thus, the dynamic ionic bonding allows AOB binder to deliver a good self-healing ability of as-prepared electrode.

Given the hierarchical structure of spidroin is highly linked with the assembly of corresponding polyamino acid segments in aqueous solutions, here, a facile aqueous-oil binary mixing process was conducted to regulate the condensed structure of AOB binder. As fair comparison, the PAA/PPB blend binders in sole water or sole NMP (denoted as PAB-W and PAB-N binder, respectively) were also prepared. To begin with, a PAA/PPB weight ratio of 3/1 was selected in the condensed structure regulation research. As depicted in Figure S5a, the PAB-N film shows a uniformly dispersed fiber morphology. After addition of water, the sample surface shows many uniformly dispersed or unequally distributed micron-sized or submicron-level irregular rod- or sphere-like clusters (Figure S5b-d). By adjusting the volume ratio of water/NMP, the condensed structure of AOB binder can be regulated. It is evident that AOB binder films prepared with a water/NMP ratio of 1/5 exhibit the medium uniformly distributed clusters; submicron-sized irregular spherical domains are observed via higher resolution SEM and top-viewed AFM height sensor imaging

analyses (Figure S6b and S7). Notably, SEM mapping demonstrates that there are much more N elements distributed in the cluster domains than the rest of the film, while C elements are relatively uniform in the AOB binder (Figure S6c-d). For further microstructure analysis of the AOB binder film, confocal laser scanning microscope (CLSM) and atomic force microscope (AFM) were performed. Apparently, distinct distribution of PPB and PAA in the AOB binder film can be observed (Figure S8). Consistent with the SEM element mapping results (Figure S6c-d), PAA is uniformly distributed in the whole film (Figure S8c), while the PPB exists more in the submicron-sized irregular spherical domains (Figure S8b); these results are highly correlated with the ionic bonding-induced co-assembly of PAA and PPB. X-ray diffraction demonstrates that there is a strong crystalline peak at 16.78° with d spacing of 5.28 \AA in the AOB binder film, in sharp contrast to that of PAB-N film (Figure S9a-b). This result clearly proves that the aqueous-oil binary mixing process renders the generation of crystalline zones in the AOB binder film. Given that PAA is amorphous (Figure S9c), it can be concluded that the crystallization domains belong to the ordered assembly of PAN segments in PPB. Furthermore, considering the oleophilic PPB distribution, the crystallization domain is prone to existing in the submicron-sized irregular spherical clusters of AOB binder films. This indicates that submicron-sized irregular spherical clusters formed by PPB within the AOB binder are, in part, stacked in order. More importantly, the crystallization peak is also present in the Si electrode with AOB binder (Figure S9d-e).

Figure 2e vividly illustrates the condensed structure formation of AOB binder via an aqueous-oil binary mixing process. In the cosolvent, by virtue of strong ionic bonding interactions between PAA and PPB, submicron-sized irregular spherical clusters can generate through the co-assembly of major PPB with minor PAA, and other PPB and PAA synergistically constitute long polymer chains that undergo physical/ionic crosslinking themselves forming the uniform domain in the AOB binder film. During this process, part of PAN segments on PPB can crystallize within the submicron-sized irregular spherical clusters. Eventually, the spider-like hierarchical structure binder with amorphous and crystallization domains is constructed. While the PAB-W film shows clusters with irregular shape, size and distribution area, which have negative impacts on the electrode particle dispersion (mentioned below).

Physical property evaluations of AOB binder

Via stress-strain curves strength analyses, the water/NMP ratio of 1/5 in the aqueous-oil binary mixing process of AOB binder samples, which renders superior mechanical properties, was chosen as the optimum one for following research (Figure S10). Additionally, it is worth mentioning that compared with PAB-N and PAB-W binder, the AOB binder renders enhanced mechanical and adhesion properties (Figure S10-11), clearly proving the significance of binder hierarchical structure design. Compared with the traditional PAA binder film, AOB binder achieves evidently enhanced tensile strength (68 vs. 21 MPa) and higher elongation at break (22.1% vs. 5.5%) (Fig. 3a). To reflect the practical mechanical properties of binders within cells, the AOB binder films were soaked in electrolyte for 24 hours. Figure 3b shows the sequential loading-unloading curves of the as-prepared electrolyte soaked AOB binder film at a strain limit of 30%. The stress and strain values remain approximately constant for four cycles, indicative of the excellent recoverable behavior of AOB binder films. Afterwards, AOB binder films can achieve a tensile

strength of 55 MPa and an elongation at the break of 58%. Superior mechanical properties of AOB binder films are also reflected in the nanoindentation test. At a given nanoindentation force (a maximum load of 500 μN), AOB binder films exhibit an evidently smaller indentation depth (479 vs. 738 nm) than PAA binder (Figure S12). Moreover, the Si electrode with AOB binder shows much higher reduced modulus (1.08 vs. 0.6 GPa) and hardness (0.08 vs. 0.03 GPa) than those of PAA binder (Fig. 3c). Enhanced mechanical properties of the as-developed binder are more favorable to decrease Si-based electrode volume expansion.³⁶

In a 180° peeling test for Si electrodes, the average peel strengths of the AOB and PAA binders based Si electrodes are 2.56 N and 0.64 N, respectively (Fig. 3d), showing the enhanced adhesion to Cu current collector. Additionally, the wettability test on Si surface was conducted to provide good insight into the affinity of binder to Si. Polymer solutions containing 1 wt% of AOB or PAA binder were dropped onto the surface of the monocrystalline silicon wafer to conduct contact angle measurements. After standing for 2 min, the contact angles of the AOB and PAA binder solutions are 39.1° and 50.6°, respectively (Figure S13), indicative of the improved wettability of the AOB binder solution. Enhanced wettability can prevent stress concentration at the interface between binder and Si anode from forming a large number of defects; this effect is effective to stabilize the Si-based electrode structure.³⁷ This observation can be explained by the higher affinity of AOB binder to the Si surface due to abundant polar groups such as carboxyl and tetrazole. Furthermore, the AOB binder film exhibits a lower swelling ratio (4% vs. 6%) of electrolytes than the PAA counterpart (Figure S14), which helps retain mechanical strength and high adhesion during battery cycling. More impressive is that AOB binder films exhibit an excellent self-healing ability. It is demonstrated that two separated AOB binder films can recover within 12 hours under room temperature (Figure S15), mainly attributed to its dynamically reversible ionic bonding network. Superior mechanical, adhesive and self-healing abilities of AOB binder are anticipated to better withstand the huge volume change of Si particles and suppress excessive volume expansion of Si-based electrodes.

Evolution of electrodes during cycling

SEM imaging was used to explore the surface morphology evolution of Si electrodes with varied binders before and after 50 cycles. As shown in Fig. 4a-b, for the pristine Si electrode, AOB binder renders more uniformly dispersed electrode particles than PAA binder, mainly due to the superior wettability of AOB binder to Si. In sharp contrast with AOB binder, PAB-W binder incurs large cluster and obvious cracks on the pristine Si electrode surface (Figure S16), which is highly correlated with its clusters with irregular shape, size and distribution area. After 50 cycles, surface SEM images show more cracks on PAA based Si electrodes, compared with the AOB binder based one (Fig. 4c-d). Furthermore, cross-sectional ion milling-scanning electron microscopy (IM-SEM) analyses present the thickness variation of Si electrodes with different binders before and after 50 cycles (Fig. 4e-h). The AOB binder-based Si electrode shows a thickness enhancement of $\sim 22\%$ (18 \rightarrow 22 μm), much smaller than that ($\sim 50\%$, 20 \rightarrow 30 μm) of PAA counterparts. Notably, there were several cracks in the cycled PAA-based electrode, in sharp contrast to the well integrity of the one with AOB binder. In addition, the thickness change of electrode during the first lithiation and delithiation process was observed through the in-situ optical microscope (OM) in real time.

It is evident that the PAA-based Si electrode thickens severely after first lithiation (Movie S1). In sharp contrast, AOB binder can better suppress electrode expansion (Movie S2). For understanding the effect of varied binders on electrode evolution during cycling, finite element simulation was carried out to investigate the contact stress on the surface of Si particles at the phase of $\text{Li}_{15}\text{Si}_4$ (Fig. 4i-k and S17). It can be seen that the Von Mises stress between adjacent Si particles in the presence of PAA binder is much higher than that (~ 2000 vs. ~ 800 MPa) of AOB binder. These results demonstrate that the AOB binder can better buffer the volume stress and thus maintain the integrity of Si anode. This is mainly ascribed to its superior mechanical properties benefited by the rational hierarchical structure design.

Decreased Si electrode expansion in the presence of AOB binder helps to maintain solid electrolyte interphase (SEI) stability. This can be reflected by surface chemical components of cycled Si electrodes characterized through X-ray photoelectron spectroscopy (XPS) measurements. In the XPS C1s spectra, one of the most noticeable differences is the intensity of the peak at 289.6 eV corresponding to electrolyte decomposition side products $\text{ROCO}_2\text{Li} / \text{Li}_2\text{CO}_3$ (Figure S18a-b);³⁸ the AOB binder based Si electrode shows a weaker signal intensity ratio than that of the one with PAA binder, demonstrating that less electrolyte decomposition occurs at the interface of the cycled AOB binder based Si electrode. Moreover, in the F 1s spectra, there were three typical peaks, LiF (685 eV), $\text{Li}_x\text{PO}_y\text{F}_z$ (687 eV) and Li_xPF_y (689 eV) (Figure S18c-d).^{38,39} Apparently, the Si electrode with AOB binder shows higher LiF, which is a crucial component of SEI offering preferable mechanical stability. The N 1s spectrum of the AOB based anode surface after 30 cycles shows a strong N–Li peak (Figure S19), corresponding to lithiation of tetrazole motifs, which is beneficial to transport lithium ions. This finding proves that AOB binder tends to participate in SEI formation. To elucidate the mechanism behind this, density functional theory (DFT) calculations were performed. As shown in Figure S20, AOB binder has the lower-lying LUMO level (-0.97 eV) than those of PAA, PPB and carbonate solvents (i.e. DMC and EC). This finding demonstrates that AOB binder would be subjected to be reduced prior to the electrolyte solvents and participate in the formation of polymer-reinforced SEI; such a function of AOB binder toughens SEI and effectively decreases electrolyte decomposition, beneficial to electrochemical performance of Si-based anodes.

Si-based electrode performance evaluations

As plotted in Figure S21, the electrochemical stability of Si/Li half-cells with AOB binder was measured via cyclic voltammetry (CV) analysis at a scan rate of 0.5 mV/s. Two broad peaks around ~ 0.37 and ~ 0.51 V correspond to the delithiation process of Li-Si phases.⁴⁰ Moreover, a reduction peak at about 0.19 V appears, assigned to the reversible lithiation process of amorphous Si domains to Li-Si phase. The intensity of these peaks increases with cycling, attributed to the formation of ion-conducting SEI, and more electrolyte permeation into electrode facilitating ionic transport (deduced via battery cycling test below). These results confirm the high electrochemical stability of AOB binder. To verify the utility of AOB binder, Si-based electrode assembled cell performance was evaluated. By measuring Si/Li battery performance, the AOB binder with a PPB/PAA weight ratio of 3:1 was selected as the optimal component ratio for further cell performance evaluations (Figure S22). Noting that compared with PAB-N and PAB-W,

AOB binder shows the improved battery cycle performance attributable to its enhanced mechanical and adhesion abilities; this clearly proves hierarchical structure design significance of AOB binder.

In coin-type half-cells, AOB binder renders much superior electrochemical performance to those of the PAA binder (Fig. 5a-d). Specifically, the AOB binder based nano-Si electrodes can retain a delithiation capacity of 1617 mAh/g in half-cells after 1000 cycles at 0.4 C under 0.005 – 1.5 V (Fig. 5a). The average Coulombic efficiency (CEs) of the AOB and PAA binders in this half-cell are 99.8% and 98.9%, respectively. Higher CEs represent fewer electrolyte decomposition side reactions in the presence of AOB binder, mainly ascribed to that its superior mechanical and adhesive properties can maintain electrode interface stability. Additionally, the AOB binder-based nano-Si electrode shows excellent rate performance (Fig. 5b), achieving a delithiation capacity of 1350 mAh/g at 2 C, evidently exceeding the PAA based one (980 mAh/g). Application superiority of AOB binder was further evidenced by stable cycling of commercial-level S600 electrode. As shown in Fig. 5c, S600 electrodes based on AOB binder deliver an initial delithiation capacity of 650 mAh/g at 0.1 C and of 539 mAh/g at 0.5 C, and then stabilize at 464 mAh/g in half-cells after 300 cycles at 0.5 C, much superior to that (230 mAh/g after 300 cycles at 0.5 C) of the PAA counterpart. At varied C-rates from 0.1 C to 2 C, AOB binder based S600 electrodes also show apparently enhanced delithiation capacity when compared with PAA (Fig. 5d). Moreover, typical galvanostatic voltage profiles of Si and S600 electrodes in half-cells present that AOB binder endows slighter battery polarization than PAA binder upon long cycling (Figure S23 and S24); this can be supported by lower impedance evolution (Figure S25 and Table S1), which is highly correlated with stable SEI enabled by AOB binder.

More impressively, in commercial-level $\text{LiNi}_{0.8}\text{Co}_{0.1}\text{Mn}_{0.1}\text{O}_2$ (NCM811) full cells, the as-developed binder enables excellent cyclabilities (Fig. 5e-j). The AOB binder based NCM811/S600 coin-type full cell (a NCM811 mass loading of 17.6 mg/cm^2) displays an areal capacity of 2.85 mAh/cm^2 at the initial 3 cycles of 0.1 C followed by stable cycling at 0.2 C in the voltage range of 3.0-4.2 V (Fig. 5e and S26). After 100 cycles at 0.2 C, the full-cell can still maintain an areal capacity of 1.48 mAh/cm^2 . Then, by extending the voltage range from 2.7 to 4.25 V, the battery can still stably cycle in following cycling. As for NCM811/nano-Si coin-type full cells (a NCM811 mass loading of 18.5 mg/cm^2), a capacity retention of 80% after 200 cycles is achieved (Fig. 5f and S27). In order to further prove the practicability of AOB binder, the 3.3Ah soft package cell (Fig. 5g) was prepared by pairing the AOB binder based S600 anode with a commercial-level NCM811 cathode (see detailed information in Table S2). The full cells were activated for 3 cycles at 0.1 C followed by charging and discharging at 1C ($1\text{C} = 600 \text{ mA/g}$) between 2.8 and 4.25 V. When cycling at 1 C, the NCM811/S600 full cell delivers an initial capacity of 3.22 Ah and still preserves a capacity of 2.92 Ah after 700 cycles (capacity loss: 0.013%/cycle, Fig. 5g and S28). Undoubtedly, electrochemical performance evaluations fully confirm that AOB binder is very valuable in practical implementation of Si-based batteries.

Furthermore, we compared the Si-based electrode cycle performance of previously reported typical binders with AOB binder in half-cells and soft package full cells (Fig. 5h-i and Table S3). Obviously, AOB

binder has the leading cycling performance of Si-based electrodes, to the best of our knowledge. These results clearly verify the hierarchical structure design rationality of AOB binder.

In summary, we develop a spidroin-inspired hierarchical structure binder to unlock the stiff challenges faced by Si-based electrode. In the structure of AOB binder, hydrophobic PPB polymer condensates with a minor part of PAA in the mixture solution to form crystalline regions within submicron-sized irregular spherical domains, functioning as the rigid node of binder mimicking β -sheet of spidroin; while amorphous PAA imitates the α -helix structure of spidroin, and builds an ionic bonding network structure with PPB, similar to the interactions between NTD and CTD in the primary structure of spidroin. Benefited by such bionics design, the as-developed AOB binder has the two following competitive edges: (1) Superior mechanical and adhesive capabilities were achieved via the hierarchical structure design including the dynamically reversible ionic bonding network. These factors help achieve energy dissipation and thus can accommodate enormous electrode volume deformation; (2) Low-lying LUMO leads to preferentially reduction, which helps form a polymer-reinforced SEI layer. As a result, AOB binder endows Si and S600 electrodes with superior electrochemical performance to traditional PAA binder, showing good potential for practical implementation of Si-based electrodes that meet the requirement of commercial-level high energy density LIBs. This work marks a milestone in achieving advanced silicon-based electrodes towards high energy lithium battery applications.

Declarations

Acknowledgements

This work was financially supported by the Finance science and technology project of hainan province (ZDKJ202014), the Key Scientific and Technological Innovation Project of Shandong (No. 2022CXGC020301), the National Natural Science Foundation of China (22139001, 22279153), the Science Foundation for the Strategic Priority Research Program of the Chinese Academy of Sciences (XDA22010603), the Taishan Scholars of Shandong Province (No. ts201511063), the Shandong Energy Institute (Grant No. SEI I202108) and the Shandong Provincial Natural Science Foundation (ZR2022QB160).

Author contributions

P. Z. Mu, H. R. Zhang, S. M. Dong and G. L. Cui. participated in conceiving and designing the experiments. P. Z. Mu performed the materials syntheses, electrochemical measurements and prepared the samples for material characterization with assistance from Z. Liu, J. D. Li. S. Zhang performed calculation. P. Z. Mu. prepared the figures and wrote the manuscript with assistance from all authors. All authors participated in discussions and know the implications of the work.

Additional information

Supplementary Information accompanies this paper at <http://www.nature.com/naturecommunications>.

Competing financial interests: The authors declare no competing financial interests.

Reprints and permission information is available online at <http://www.nature.com/naturecommunications>.

References

1. Xiang, J. *et al.* Alkali-metal anodes: from lab to market. *Joule* **3**, 2334-2363 (2019).
2. Armand, M. & Tarascon, J.-M. J. N. Building better batteries. *Nature* **451**, 652 (2008).
3. Scrosati, B. & Garche, J. Lithium batteries: status, prospects and future. *J. Power Sources* **195**, 2419-2430, (2010).
4. Kim, S. *et al.* A “sticky” mucin-inspired DNA-polysaccharide binder for silicon and silicon–graphite blended anodes in lithium-ion batteries. *Adv. Mater.* **30**, 1707594 (2018).
5. Ryu, J. *et al.* Room-temperature crosslinkable natural polymer binder for high-rate and stable silicon anodes. *Adv. Funct. Mater.* **30**, 1908433 (2020).
6. Franco Gonzalez, A., Yang, N.-H. & Liu, R.-S. Silicon anode design for lithium-ion batteries: progress and perspectives. *J. Phys. Chem. C* **121**, 27775-27787 (2017).
7. Chen, H. *et al.* A mechanically robust self-healing binder for silicon anode in lithium ion batteries. *Nano Energy* **81**, 105654 (2021).
8. Son, Y. *et al.* Exploring critical factors affecting strain distribution in 1D silicon-based nanostructures for lithium-ion battery anodes. *Adv. Mater.* **30**, 1705430 (2018).
9. Choi, S. *et al.* Highly elastic binders integrating polyrotaxanes for silicon microparticle anodes in lithium ion batteries. *Science* **357**, 279-283 (2017).
10. Chen, J. *et al.* Electrolyte design for LiF-rich solid–electrolyte interfaces to enable high-performance micro-sized alloy anodes for batteries. *Nat. Energy* **5**, 386-397 (2020).
11. Kwon, T. W., Choi, J. W. & Coskun, A. The emerging era of supramolecular polymeric binders in silicon anodes. *Chem. Soc. Rev.* **47**, 2145-2164 (2018).
12. Zou, F. & Manthiram, A. A review of the design of advanced binders for high-performance batteries. *Adv. Energy Mater.* **10**, 2002508 (2020).
13. Jeong, Y. K. *et al.* Millipede-inspired structural design principle for high performance polysaccharide binders in silicon anodes. *Energy Environ. Sci.* **8**, 1224-1230 (2015).
14. Magasinski, A. *et al.* Toward efficient binders for Li-ion battery Si-based anodes: polyacrylic acid. *ACS Appl. Mater. Interfaces* **2**, 3004-3010 (2010).
15. Choi, N.-S. *et al.* Enhanced electrochemical properties of a Si-based anode using an electrochemically active polyamide imide binder. *J. Power Sources* **177**, 590-594 (2008).
16. Xu, Z. *et al.* Silicon microparticle anodes with self-healing multiple network binder. *Joule* **2**, 950-961 (2018).

17. Jeong, Y. K., Park, S. H. & Choi, J. W. Mussel-inspired coating and adhesion for rechargeable batteries: a review. *ACS Appl. Mater. Interfaces* **10**, 7562-7573 (2018).
18. Chen, H. *et al.* Exploring chemical, mechanical, and electrical functionalities of binders for advanced energy-storage devices. *Chem. Rev.* **118**, 8936-8982 (2018).
19. Zhao, Y. *et al.* Rational design of functional binder systems for high-energy lithium-based rechargeable batteries. *Energy Storage Mater.* **35**, 353-377 (2021).
20. Han, Z. J., Yabuuchi, N., Hashimoto, S., Sasaki, T. & Komaba, S. Cross-linked poly(acrylic acid) with polycarbodiimide as advanced binder for Si/graphite composite negative electrodes in Li-ion batteries. *ECS Electrochem. Lett.* **2**, A17-A20 (2012).
21. Koo, B. *et al.* A highly cross-linked polymeric binder for high-performance silicon negative electrodes in lithium ion batteries. *Angew Chem. Int. Ed. Engl.* **124**, 8892-8897 (2012).
22. Wang, C. *et al.* Self-healing chemistry enables the stable operation of silicon microparticle anodes for high-energy lithium-ion batteries. *Nat. Chem.* **5**, 1042-1048 (2013).
23. Guo, M.-J. *et al.* A dual force cross-linked γ -PGA-PAA binder enhancing the cycle stability of silicon-based anodes for lithium-ion batteries. *Electrochim. Acta* **425**, 140704 (2022).
24. Wang, Y., Xu, H., Chen, X., Jin, H. & Wang, J. Novel constructive self-healing binder for silicon anodes with high mass loading in lithium-ion batteries. *Energy Storage Mater.* **38**, 121-129 (2021).
25. Kang, S., Yang, K., White, S. R. & Sottos, N. R. Silicon composite electrodes with dynamic ionic bonding. *Adv. Energy Mater.* **7**, 1700045 (2017).
26. Pan, Y., Gao, S., Sun, F., Yang, H. & Cao, P. F. Polymer binders constructed through dynamic noncovalent bonds for high-capacity silicon-based anodes. *Chemistry* **25**, 10976-10994 (2019).
27. Zhao, J. *et al.* A photoenhanced oxidation of amino acids and the cross-linking of lysozyme mediated by tetrazolium salts. *Phys. Chem. Chem. Phys.* **23**, 3761-3770 (2021).
28. Maldonado, F., Packard, T. T. & Gómez, M. Understanding tetrazolium reduction and the importance of substrates in measuring respiratory electron transport activity. *J. Exp. Mar. Biol. Ecol.* **434-435**, 110-118 (2012).
29. Nineham, A. W. The chemistry of formazans and tetrazolium salts. *Chem. Rev.* **55**, 355-483 (1955).
30. Yan, C. *et al.* Significantly improving lithium-ion transport via conjugated anion intercalation in inorganic layered hosts. *ACS Nano* **12**, 8670-8677 (2018).
31. Liao, X. *et al.* High strength in combination with high toughness in robust and sustainable polymeric materials. *Science* **366**, 1376-1379 (2019).
32. Wang, Q. *et al.* High-performance micro-sized Si anodes for lithium-ion batteries: insights into the polymer configuration conversion mechanism. *Adv. Mater.* **34**, 2109658 (2022).
33. Sexton, B. A. & Avery, N. R. Coordination of acetonitrile (CH_3CN) to platinum (111): evidence for an $\eta^2(\text{C}, \text{N})$ species. *Surf. Sci.* **129**, 21-36 (1983).
34. Hu, L. *et al.* Gradient H-bonding binder enables stable high-areal-capacity Si-based anodes in pouch cells. *Adv. Mater.* **33**, 2104416 (2021).

35. Ikura, R. *et al.* Design of self-healing and self-restoring materials utilizing reversible and movable crosslinks. *NPG Asia Mater.* **14**, 10 (2022).
36. Jiang, M. *et al.* An endotenon sheath-inspired double-network binder enables superior cycling performance of silicon electrodes. *Nano-Micro Lett.* **14**, 87 (2022).
37. Hosokawa, H., Shimojima, K., Matsumoto, A., Kato, K. & Matsubara, H. Wettability of Ni/(Ti_xMe_{1-x}) (CuNv) system (Me=Mo, W). *Int. J. Refract. Met. H.* **33**, 1-5 (2012).
38. Wu, S. *et al.* In-situ polymerized binder: a three-in-one design strategy for all-integrated SiO_x anode with high mass loading in lithium ion batteries. *ACS Energy Lett.* **6**, 290-297 (2020).
39. Nölle, R., Schmiegel, J.-P., Winter, M. & Placke, T. Tailoring electrolyte additives with synergistic functional moieties for silicon negative electrode-based lithium ion batteries: a case study on lactic acid O-carboxyanhydride. *Chem. Mater.* **32**, 173-185 (2019).
40. Yan, J. *et al.* Artificial solid electrolyte interphase coating to reduce lithium trapping in silicon anode for highly stable lithium storage. *Surf. Interfaces* **31**, 102029 (2022).
41. Cao, P.-F. *et al.* Rational design of a multifunctional binder for high-capacity silicon-based anodes. *ACS Energy Lett.* **4**, 1171-1180 (2019).
42. Jin, B. *et al.* A self-healable polyelectrolyte binder for highly stabilized sulfur, silicon, and silicon oxides electrodes. *Adv. Funct. Mater.* **31**, 2104433 (2021).
43. Li, J. *et al.* A novel multi-functional binder based on double dynamic bonds for silicon anode of lithium-ion batteries. *Electrochim. Acta* **425**, 140620 (2022).
44. Li, Z. *et al.* A robust network binder via localized linking by small molecules for high-areal-capacity silicon anodes in lithium-ion batteries. *Nano Energy* **79**, 105430 (2021).
45. Jung, C. H., Kim, K. H. & Hong, S. H. Stable silicon anode for lithium-ion batteries through covalent bond formation with a binder via esterification. *ACS Appl. Mater. Interfaces* **11**, 26753-26763 (2019).
46. He, J. & Zhang, L. Polyvinyl alcohol grafted poly (acrylic acid) as water-soluble binder with enhanced adhesion capability and electrochemical performances for Si anode. *J. Alloys Compd.* **763**, 228-240 (2018).
47. Wu, H. *et al.* Stable Li-ion battery anodes by in-situ polymerization of conducting hydrogel to conformally coat silicon nanoparticles. *Nat. Commun.* **4**, 1943 (2013).
48. Yuca, N. *et al.* Highly efficient poly(fluorene phenylene) copolymer as a new class of binder for high-capacity silicon anode in lithium-ion batteries. *Int. J. Energy Res.* **42**, 1148-1157 (2018).
49. Li, Z. *et al.* Silicon anode with high initial coulombic efficiency by modulated trifunctional binder for high-areal-capacity lithium-ion batteries. *Adv. Energy Mater.* **10**, 1903110 (2020).
50. Li, Z. *et al.* An ion-conductive grafted polymeric binder with practical loading for silicon anode with high interfacial stability in lithium-ion batteries. *Adv. Energy Mater.* **12**, 2201197 (2022).
51. Bai, M. *et al.* Encasing prelithiated silicon species in the graphite scaffold: an enabling anode design for the highly reversible, energy-dense cell model. *ACS Appl. Mater. Interfaces* **12**, 47490-47502 (2020).

52. Han, X. *et al.* On the interface design of Si and multilayer graphene for a high-performance Li-ion battery anode. *ACS Appl. Mater. Interfaces* **12**, 44840-44849 (2020).
53. Liu, T. *et al.* Interweaving 3D network binder for high-areal-capacity Si anode through combined hard and soft polymers. *Adv. Energy Mater.* **9**, 1802645 (2019).
54. Zhao, L. *et al.* Compact Si/C anodes fabricated by simultaneously regulating the size and oxidation degree of Si for Li-ion batteries. *J. Mater. Chem. A* **7**, 24356-24365 (2019).
55. Qi, C. *et al.* Suitable thickness of carbon coating layers for silicon anode. *Carbon* **186**, 530-538 (2022).
56. Song, J. *et al.* Suppressed volume variation of optimized SiO_x/C anodes with PAA-based binders for advanced lithium-ion pouch cells. *Solid State Ion* **343**, 115070 (2019).

Figures

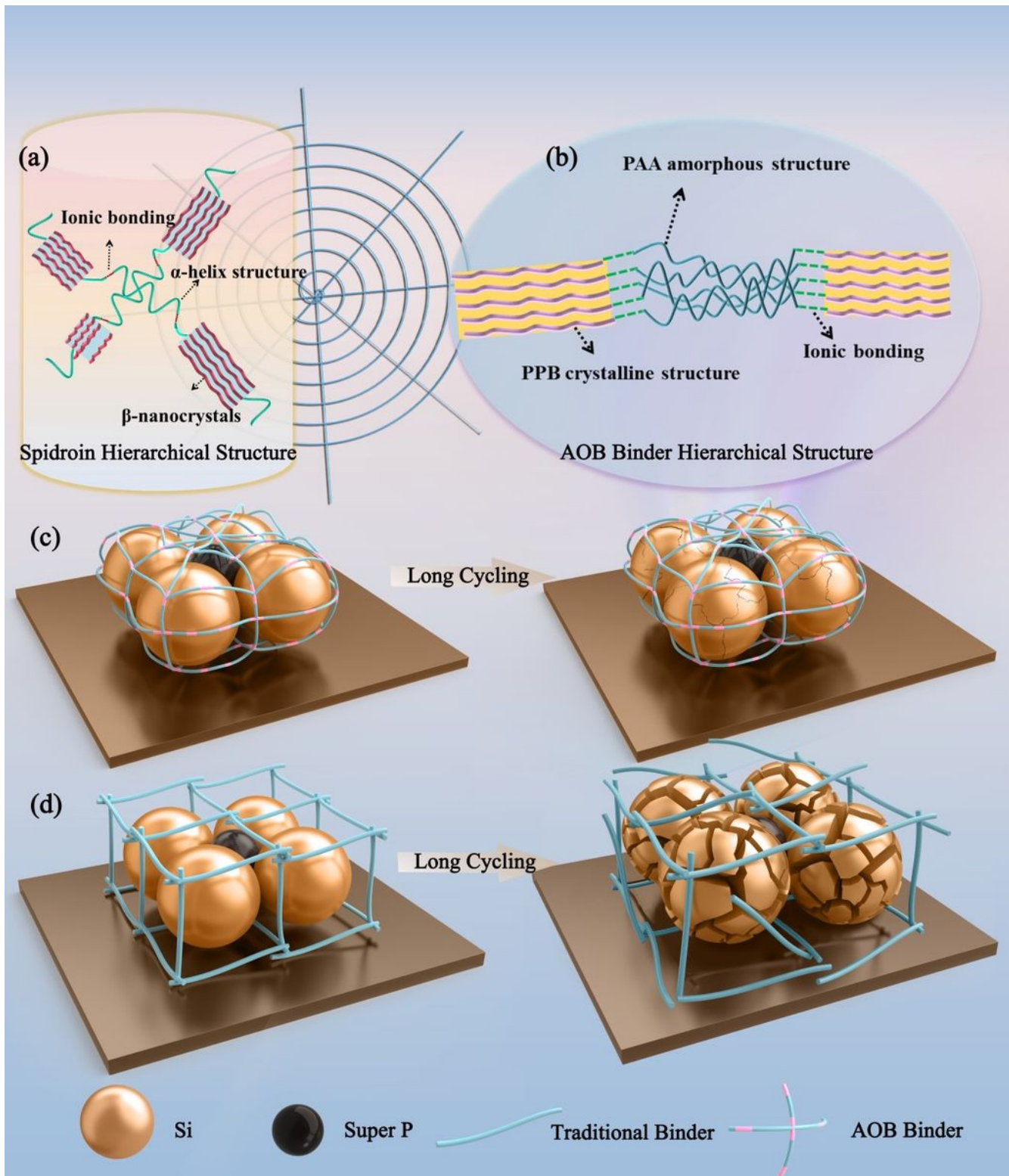


Figure 1

Schematic illustration of (a) the hierarchical structure of spidroin, (b) the hierarchical structure of AOB binder, and Si based electrode evolution using the (c) traditional binder and (d) AOB binder during long cycling.

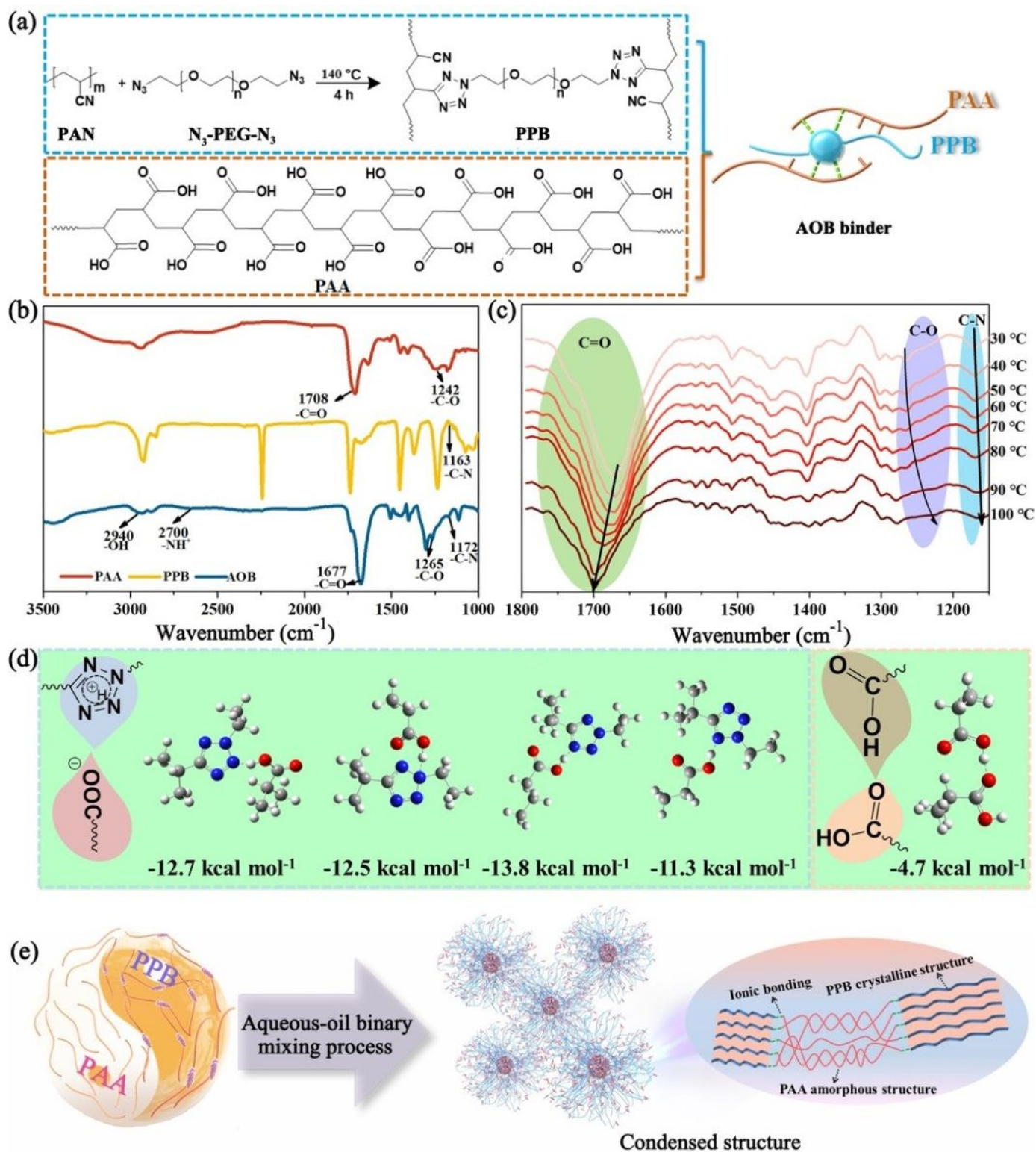


Figure 2

(a) Schematic diagrams of PPB synthesis, PAA structure and AOB binder constitution. (b) FTIR spectra of PAA, PPB, and AOB binder. (c) Temperature-dependent FTIR spectrum of AOB binder with a wavenumber range from 1800 to 1150 cm^{-1} . (d) Bonding types and bond energies calculated by DFT simulations. (e) The condensed structure formation of AOB binder via an aqueous-oil binary mixing process.

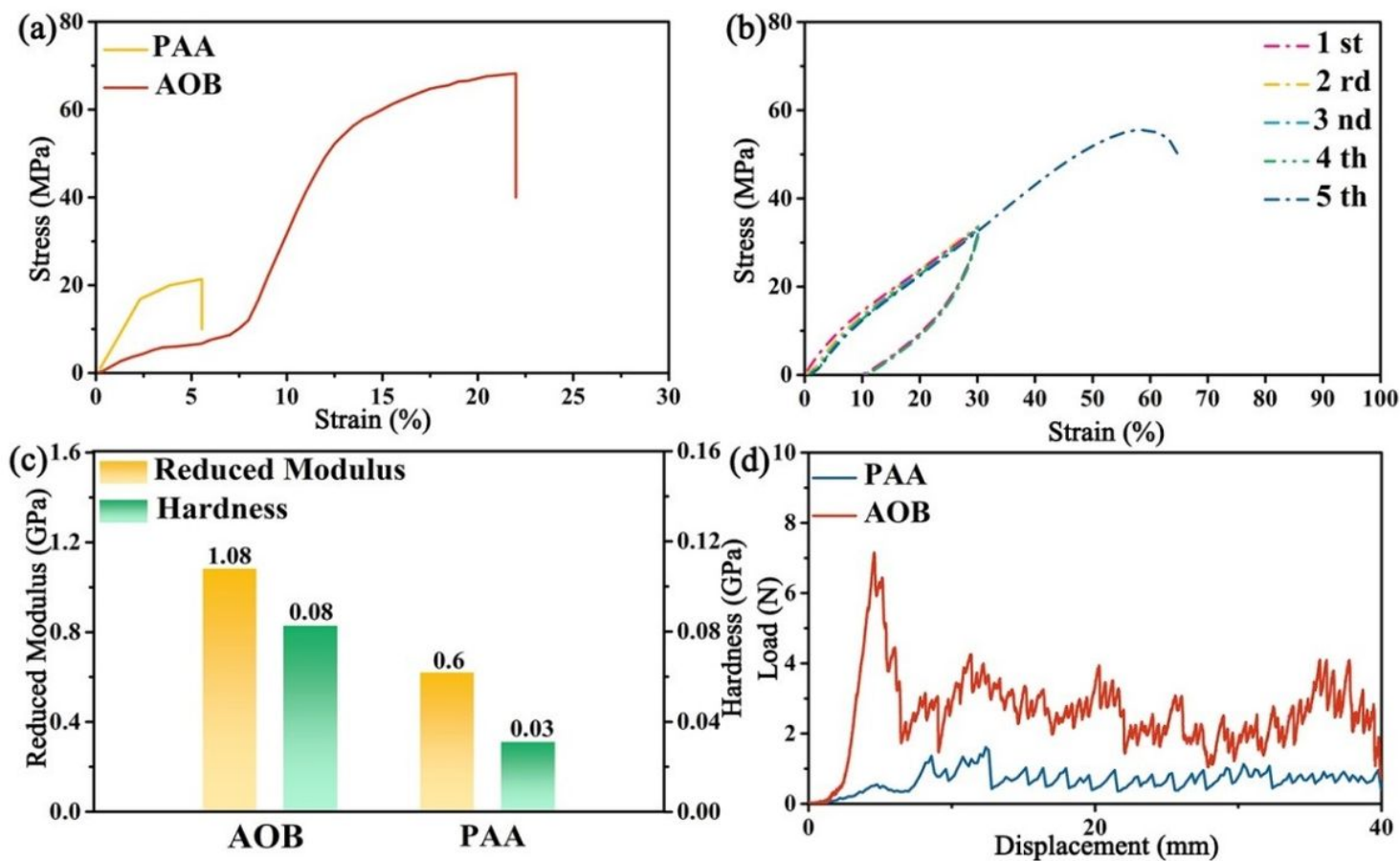


Figure 3

(a) Stress-strain curves of PAA and AOB binder membranes. (b) Successive loading-unloading curves of the as-prepared electrolyte soaked AOB binder film at a strain limit of 30%. (c) Reduced modulus and hardness of Si electrodes with varied binders obtained from nanoindentation tests. (d) Peeling force-displacement curves of Si electrodes with PAA and AOB binders.

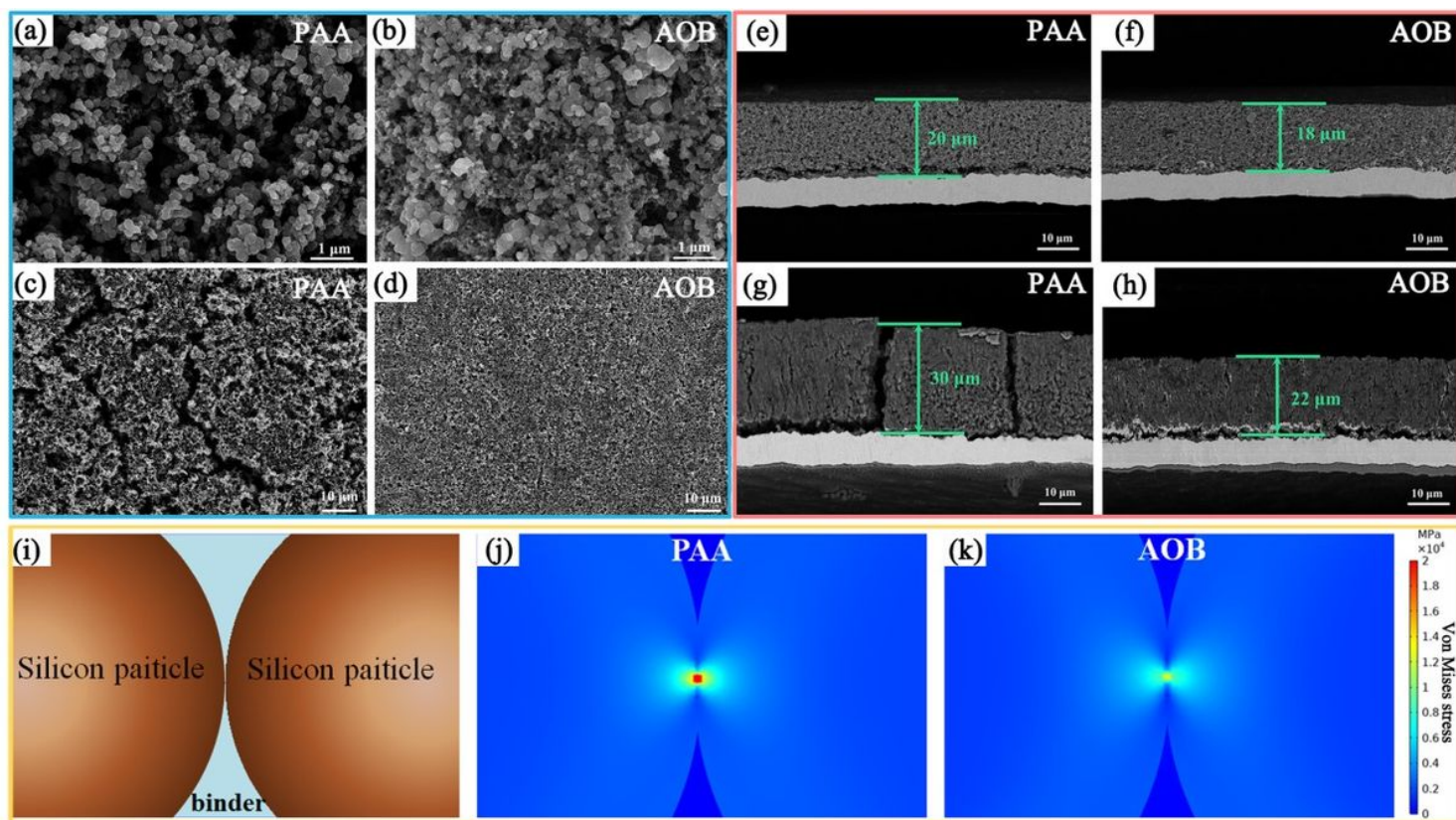


Figure 4

Top-viewed SEM images of the (a, b) pristine Si electrodes and (c, d) the ones after 50 cycles with PAA and AOB binders. Cross-sectional IM-SEM images of Si electrodes (e, f) before and (g, h) after 50 cycles with PAA binder and AOB binder. (i) The regular symmetry finite element model between adjacent Si particles. Contour plots of Von Mises stress between adjacent Si particles in the presence of (j) PAA binder and (k) AOB binder at $\text{Li}_{15}\text{Si}_4$ phase in regular symmetry finite element model.

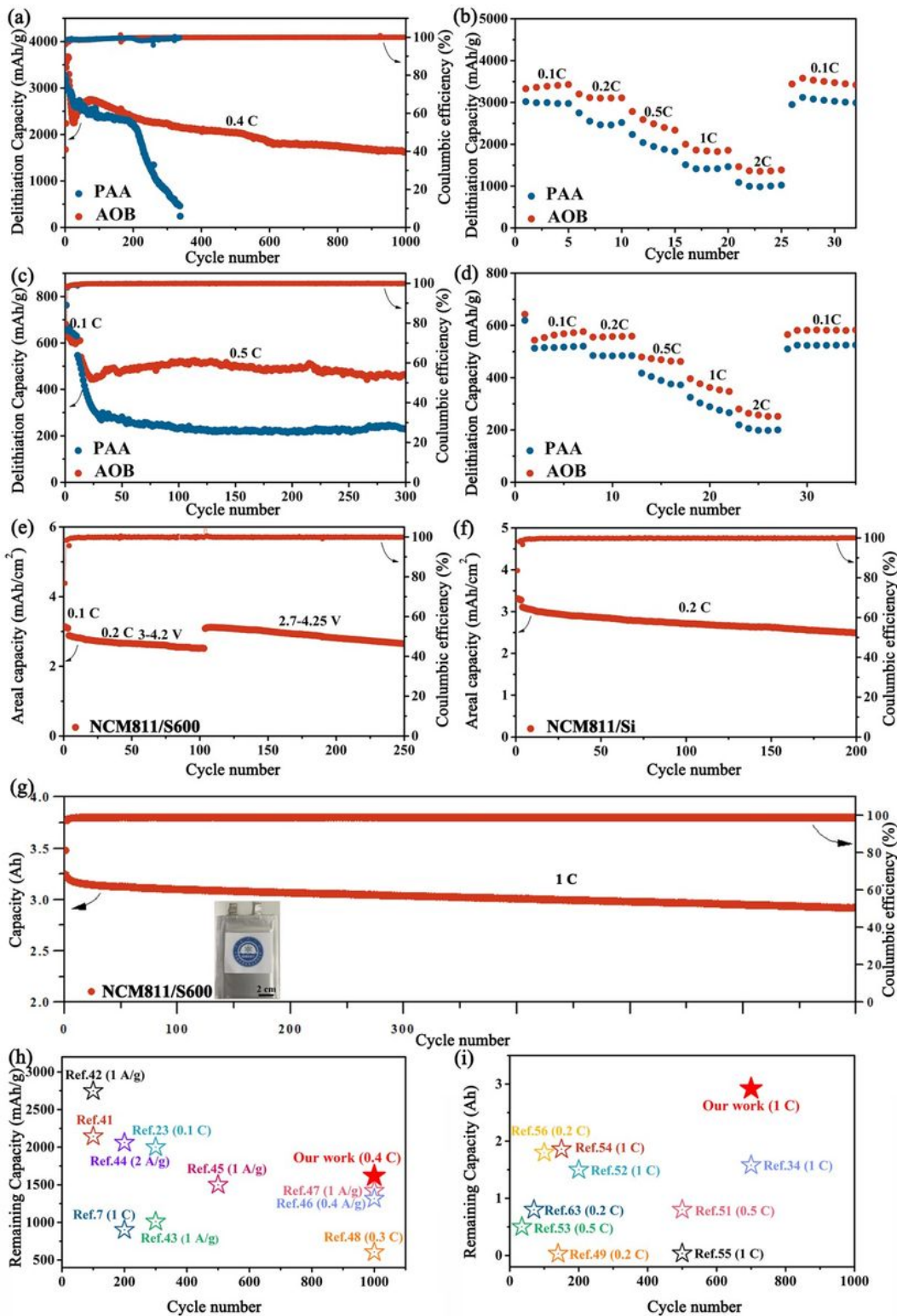


Figure 5

(a) Long-term cycling performance at 0.4 C and (b) rate capability of varied binders-based nano-Si electrode (a mass loading of 0.8 mg cm^{-2}) assembled coin-type half-cells under 0.005-1.5 V. (c) Long-term cycling performance at 0.5 C and (d) rate capability of varied binders-based S600 electrode (a mass loading of 4 mg/cm^2) in coin-type half-cells under 0.005-1.5 V. (e) Cycling performance of NCM811/AOB binder based S600 coin-type full cell (a NCM811 loading of 17.6 mg/cm^2) under 3-4.2 V and then under

2.7-4.25 V at 0.2 C. (f) Cycling performance of NCM811/AOB binder based nano-Si coin-type full cells (a NCM811 loading of 18.5 mg/cm²) under 3-4.2 V at 0.2 C. (g) Photograph of NCM811/S600 soft package cells (a NCM811 loading of 18.5 mg/cm² and a S600 loading of 5.5 mg/cm² on each side) and cycling performance of such soft package full cells at 1 C under 2.8-4.25 V. Si-based electrode cycle performance comparison among AOB binder and previously reported binders in (h) half cells and (i) soft package full cells. ^{7,23,34,41-56}

Supplementary Files

This is a list of supplementary files associated with this preprint. Click to download.

- [MovieS1.mp4](#)
- [MovieS2.mp4](#)
- [SupporttingInformation.docx](#)